

Stable and Catalytically Active Shape-Engineered Cerium Oxide Nanorods by Controlled Doping of Aluminum Cations

Haoming Yan^{a‡}, Zhongqi Liu^{b‡}, Shize Yang^{c‡}, Xiaozhou Yu^a, Tao Liu^b, Qianying Guo^{b,d}, Junhao Li^b, Ruigang Wang^{b*}, and Qing Peng^{a*}

^aDepartment of Chemical and Biological Engineering, The University of Alabama, Tuscaloosa, AL 35487; ^bDepartment of Metallurgical and Materials Engineering, The University of Alabama, Tuscaloosa, AL 35487; ^cMaterials Science and Technology Division, PO BOX 2008, Oak Ridge National Laboratory, Oak Ridge, TN 37831-6071; ^dCenter for Nanophase Materials Sciences, PO BOX 2008, Oak Ridge National Laboratory, Oak Ridge, TN 37831-6071.

[‡]All authors contribute equally to this work.

^{*}Corresponding Author: rwang@eng.ua.edu; qpeng2@eng.ua.edu

ABSTRACT

Shape-engineered nanocrystals (SENs) promise a better selectivity and a higher activity in catalytic reactions than the corresponding non-shape-engineered ones owing to their larger specific surface areas and desirable crystal facets. However, often, it is challenging to apply SENs in practical catalytic applications at high reaction temperatures to achieve favorable kinetics because these desirable surface facets in SENs have higher specific surface energies than other types of facets. In this paper, we show that atomic layer deposition (ALD) of Al_2O_3 at 200 °C can controllably dope Al cations into the shape-engineered CeO_2 nanorods (NRs) to not only increase their shape transition temperature from 400 °C to at least 700 °C, but also greatly increase their specific reversible oxygen storage capacity (srOSC). The substituted Al^{3+} ions impede the surface diffusion of Ce ions, therefore improve the thermal stability of CeO_2 NRs. Al^{3+} dopants form -Al-O-Ce-O- clusters, which are new Ce specie and can be reversibly reduced and oxidized at 500 – 700 °C. Our method presents a controllable low temperature doping strategy with vapor reactants to improve the thermal stability and catalytic activities of SENs, thereby expand their applications into high temperature environments.

KEYWORDS: shape-engineered, ceria, controllable doping, atomic layer deposition, stability

INTRODUCTION

Cerium oxide (CeO_2) plays important roles as catalysts and/or catalyst supports in a wide range of applications, including three-way catalysts on catalytic converters of cars,¹ catalysts for fluidized-bed catalytic cracking,² catalytic oxidation of soot from diesel engines,³ and solid oxide fuel cells,^{4, 5} to name a few. All of these applications utilize CeO_2 because it has an exceptionally large specific (per unit mass of CeO_2) reversible oxygen storage capacity (srOSC), which originates from the redox reactions: $2\text{Ce}_2\text{O}_3 + \text{O}_2 \rightleftharpoons 4\text{CeO}_2$.¹ These practical applications demand not only a large srOSC but also a facile redox kinetics, *i.e.*, a large amount of srOSC that can be extracted at a lower temperature at a faster rate.^{4, 6-15} The redox kinetics of pure CeO_2 depends strongly on its size, shape, and crystal facets.^{12, 16-19} In comparison with other types of CeO_2 nanomaterials, shape-engineered CeO_2 nanorods (NRs) has more facile redox kinetics for srOSC,^{12, 16, 18, 19} owing to their unique physiochemical properties, including *(i)* the high density of {100} and {110} facets, which are more reducible than {111} facets;^{12, 19-21} *(ii)* the high density of defects.^{1, 12, 15, 22-24} However, these shape-engineered CeO_2 NRs permanently lose their facile redox kinetics if heated above 400 °C, because they deform into thermally more stable octahedrons, which have {111} as the dominating surface facets, and aggregate.^{15, 23, 25-27} This inferior thermal stability severely limits their applications in high temperature environments achieve fast reaction kinetics. Currently, there is no effective methods that can improve the thermal stability of these CeO_2 NRs without deforming their shapes and sizes.

The poor thermal stability of highly active shape-engineered nanocrystals SENSs, including CeO_2 NRs, is due to the diffusion of surface and bulk atoms.²⁸⁻³⁰ In order to diffuse, atoms need to break and reform bonds with surround atoms.³¹ Diffusion of a surface atom is activated at lower temperatures than diffusion of a bulk atom because surface atoms have fewer bonds with the surrounding atoms than atoms in bulk. Therefore, it is possible to improve the thermal stability of SENSs by suppressing the diffusion of surface atoms through surface modification.

Currently, the main strategies to improve the thermal stability of nanomaterials is through doping or physical confinement. For doping CeO_2 , previous methods mixed precursors of dopants and Ce in solution and calcined at high temperatures (such as 700 °C) to activate these dopants.^{8, 43, 47-48} These methods generally produce doped CeO_2 of spherical particles, which do not have the desired surface facets and nanoscale structures and do not have reducible oxygen at low temperatures, e. g., at 400 °C. In addition, such method cannot be used to dope CeO_2 nanorods, as they deform at temperature above 400 °C. Doping can also be induced through coating followed by solid state diffusion. For example, MnOx atomic layer deposition and the post annealing were used to dope Mn into TiO_2 nanowire arrays.³² Such method need high temperatures to drive the solid-state reactions in activating the dopants. This method could also potentially deform the shape-engineered nanostructures. Physical confinement has also been used to improve the stability of nanomaterials. For instance, conformal Al_2O_3 overcoating followed by thermally induced cracking³³ has been used to stabilized nanoparticles. Such conformal overcoating could deactivate the desired surface facets in shape-engineered nanomaterials. Therefore, it is challenging to apply these methods to shape-engineered nanomaterials to improve their thermal stability without sacrificing their shape-engineered structures and crystal facets.

In this paper, we present a new strategy that not only maintains the facile low temperature redox kinetics of srOSC of shape-engineered CeO_2 NRs, but also improves their thermal stability to at least 700 °C so that a large amount of sub-surface and bulk oxygen can be extracted as well. Our method is to controllably dope these shape-engineered CeO_2 NRs with low temperature atomic layer deposition (ALD). Because the unique delayed nucleation of ALD Al_2O_3 on dehydrated CeO_2 NRs, Al^{3+} cations dope onto CeO_2 NRs through reaction with trimethyl aluminum at 200 °C and substitute some Ce ions on the surface of NRs while not fully cover the surface of NRs to deactivate their useful srOSC. The controllably doped Al cations reduce the diffusion of Ce atoms by increasing the strength and number of chemical coordination of surface ions, which

block or increase the tortuosity of pathways in the diffusion of Ce ions. In contrast, CeO₂ NRs lose their low temperature oxygen storage capacity after a conformal Al₂O₃ coating at 75 °C followed by a high temperature annealing, which suggests that high temperature solid state diffusion can not activate Al dopant while maintain low temperature srOSC of CeO₂ NRs. Our method can controllably doped CeO₂ NRs at low temperature while maintain their crystal structure, shape and size, and enhance their srOSC, which is difficult to be done by previous methods.

RESULTS

Improved shape stability of shape-engineered CeO₂ NRs upto 700 °C.

Figure 1 shows the low magnification TEM images of CeO₂ NRs followed by various treatments. Figure 1a shows a typical TEM image of shape-engineered CeO₂ NRs sample, which consists mainly of rods and the amount of other shapes is negligible. There is variation in the aspect ratios of CeO₂ NRs. These shape-engineered CeO₂ NRs were synthesized at temperatures lower than 100 °C (details in the experimental section). As presented in Figure 1b, these CeO₂ NRs lose their rod shapes and transform into spherical or irregular-shaped nanoparticles after annealing at 700 °C in air for 5h (this treatment is named as HT: high temperature treatment), suggesting that these CeO₂ NRs are thermally unstable. The morphology change is consistent with literature observation of the CeO₂ NRs that are synthesized through the same method.^{26, 27} The microstructures of CeO₂NRs_HT were also analyzed by STEM (Figure S1). The main surface facet of these large nanoparticles is {111}, which is thermodynamically more stable than {110} and {100} facets but does not have low temperature oxygen storage capability.^{12, 16-19} The deformation and aggregation of CeO₂ NRs owing to the thermal diffusion of Ce.^{34, 35} This shape transformation is consistent with the result in Figure 1b.

Figure 1c show that 45 cycles of Al₂O₃ ALD do not alter the rod morphology of CeO₂ NRs. Therefore, the ALD reaction temperature (200 °C) and the ALD chemistry do not affect the morphology of the sample. For convenience, we name CeO₂ NRs after n cycles of Al₂O₃ ALD treatment as CeO₂NRs/nAl₂O₃ in the following text. Figure 1d show that CeO₂NRs/45Al₂O₃ preserved its rod shape after annealed at 700 °C in air for 5h. We name this sample as CeO₂NRs/45Al₂O₃_HT. In comparison with the results in Figure 1b, the results in Figure 1d indicate that 45-cycle ALD Al₂O₃ treatment dramatically improves the thermal stability of the CeO₂ NRs. Figure 1e-1f present the morphology of the samples of CeO₂NRs/10Al₂O₃_HT and CeO₂NRs/1Al₂O₃_HT. CeO₂NRs/1Al₂O₃_HT has numerous spherical nanoparticles, while

CeO₂NRs/10Al₂O₃_HT has negligible spherical nanoparticles. Therefore, we conclude that ALD Al₂O₃ treatment can improve the morphology stability of shape-engineered CeO₂ NRs and the degree of stability enhancement depends on the number of ALD cycles.

High resolution scanning transmission electron microscopy (STEM) images were taken to understand the effect of Al₂O₃ ALD treatment on the detailed microstructure of CeO₂ NRs. Figure 2a and 2b show that CeO₂ NRs grow along the {110} direction with side surfaces of {100} and {110}. In addition, these CeO₂ NRs are well crystallized before ALD process. The figures show that these shape-engineered CeO₂ NRs have surface defects, which could contribute to the facile oxygen redox kinetics. As shown by Figure 2c and 2d, CeO₂NRs/45Al₂O₃ still maintain {110} as the main axial and {100} and {110} as the surface facets along the sides of the CeO₂ NRs. However, we do not observe an amorphous Al₂O₃ shell around the CeO₂ NRs. This result is surprising because 45 ALD cycles could produce amorphous Al₂O₃ shell of ~ 4-5 nm if Al₂O₃ ALD follows the typical steady state growth rate of Al₂O₃ ALD, which is around 1 Å/cycle at 200 °C.³⁶ Therefore, the nucleation of Al₂O₃ ALD is not typical and significantly delayed and we will discuss it in detail in later sections.

The distribution of diameters of the shape-engineered CeO₂ NRs, CeO₂NR_HT, CeO₂NRs/45Al₂O₃, and CeO₂NRs/45Al₂O₃_HT were measured and summarized in Figure 3. CeO₂NRs/45Al₂O₃ and CeO₂NRs/45Al₂O₃_HT have a similar average diameter as CeO₂ NRs. CeO₂NRs_HT has a much larger diameter than the CeO₂ NRs and CeO₂NRs/45Al₂O₃_HT. This result further confirmed that the ALD Al₂O₃ treatment can stabilize the morphology of CeO₂ NRs at high temperatures, i.e., 700 °C in this study.

Improved specific reversible oxygen storage capacity of shape-engineered CeO₂ NRs

ALD Al₂O₃ can stabilize the shape of CeO₂ NRs, it is more important and interesting to find out how ALD Al₂O₃ affects the srOSC of the CeO₂ NRs. Figure 4 presents the H₂ consumption result (measured by hydrogen temperature programmed reduction, H₂-TPR, details in

experimental section) as a function of temperature for the pure CeO₂ NRs and the CeO₂ NRs after various treatments. The integrated area below the curve represents the amount of H₂ consumption, *i. e.*, the amount of oxygen that can be extracted by H₂. As illustrated by the curve of 1st H₂-TPR cycle of CeO₂ NRs (Figure 4a), the reduction of fresh CeO₂ NRs by H₂ takes off around 260 °C, peaks at 480 °C, and ends at ~ 580 °C. The second reduction peak takes off at 580 °C and ascends to 700 °C, which is the unbound temperature for the TPR experiment. The low temperature reduction peaked at 480 °C is ascribed to the consumption of H₂ by surface oxygen on CeO₂ NRs. The reduction at higher temperature (>580 °C) is due to H₂ that reacts with the bulk oxygen inside of CeO₂ NRs. This H₂ consumption behavior matches well with literature results of fresh CeO₂ NRs that are prepared in the similar way.^{12, 18, 37} After cooling the sample down and leaving in air for a day at room temperature, we ran the 2nd cycle of H₂-TPR for the sample, whose reduction behavior differs dramatically from that in the 1st H₂-TPR cycle. Although the H₂ consumption still takes off at 260 °C, the height of the 1st peak, which now shifts to 420 °C, decreased dramatically. The 2nd reduction peak also decreased a lot. This reduction behavior is similar as that of CeO₂NRs_HT (Figure 4a), except that CeO₂NRs_HT sample has a higher initial reduction temperature and much less H₂ consumption, *i.e.*, the specific quantity of reducible oxygen, because HT treatment deforms the shape-engineered CeO₂ NRs into spherical or irregular-shaped nanoparticles. According to these results, annealing fresh CeO₂ NRs at 700 °C in N₂ or H₂ will irreversibly damage the oxygen species that can be reduced at low temperatures. Figure 4a also illustrates how the number of ALD Al₂O₃ cycles affects the srOSC of CeO₂ NRs by comparing the TPR curves from CeO₂NRs/1Al₂O₃_HT, CeO₂NRs/10Al₂O₃_HT, and CeO₂NRs/45Al₂O₃_HT. CeO₂NRs/1Al₂O₃_HT shows a small H₂ consumption peak at ~480 °C. CeO₂NRs/10Al₂O₃_HT has two H₂ consumption peaks at 420 °C and 550 °C and has a much larger amount of reducible oxygen than CeO₂NRs/1Al₂O₃_HT. The peak at 550 °C is from a large amount of new types of oxygen species that can be reduced between 500 – 700 °C. CeO₂NRs/45Al₂O₃_HT has a similar H₂-TPR profile as that of CeO₂NRs/10Al₂O₃_HT, but a larger

srOSC than CeO₂NRs/45Al₂O₃_HT upto 700 °C. In summary, Figure 4a show that ALD Al₂O₃ treatment increases the specific **reversible** OSC in CeO₂ NRs upto 700°C and the degree of improvement increases with number of ALD cycles.

CeO₂NRs/45Al₂O₃_HT shows a dramatically different TPR behavior than CeO₂ NRs. *First*, the most significant feature is that CeO₂NRs/45Al₂O₃_HT maintained a stable H₂-TPR profile, *i.e.*, stable srOSC, as evidenced by the 1st-10th TPR cycles of the sample (Figure 4b). TPR up to 700 °C did not damage its srOSC. The exposure to air at room temperature can quickly replenish oxygen back into the H₂-reduced CeO₂NRs/45Al₂O₃_HT. The low temperature reduction (peaked ~ 480 °C) is higher in 1st TPR cycle than that in 2-10 cycles of TPR. The peak at 550 °C improves as well, meaning that the material changes into a more stable form in 1st TPR cycle. *Second*, although CeO₂NRs/45Al₂O₃_HT has a smaller peak at ~450 °C than that the 1st TPR cycle of the fresh CeO₂ NRs (not annealed by HT), it consumes a much higher amount of H₂ at 450 - 600 °C, according to the area underneath the TPR curve. This result suggests CeO₂NRs/45Al₂O₃_HT has a much larger srOSC than fresh CeO₂ NRs at temperature below 700 °C. *Third*, CeO₂NRs/45Al₂O₃_HT contains a much larger srOSC than CeO₂NRs_HT. According to these results, we conclude that CeO₂NRs/45Al₂O₃_HT has a much larger srOSC than pristine CeO₂ NRs upto 700 °C and has new oxygen species that can be reduced by H₂ between 500 °C and 600 °C, which benefits applications demanding intermediate temperature below 700 °C, such as intermediate-temperature fuel cells.

Chemical composition of CeO₂NRs/45Al₂O₃ with and w/o HT treatment

As TEM analyses of CeO₂NRs/45Al₂O₃ cannot clearly differentiate Al₂O₃ coating from CeO₂ NRs, we analyzed the nanoscale chemical composition of nanorods by HAADF-EDX mapping for samples of CeO₂NRs/45Al₂O₃ and CeO₂NRs/45Al₂O₃_HT. Figure 5a and 5e show the morphology of CeO₂NRs/45Al₂O₃ and CeO₂NRs/45Al₂O₃_HT respectively, confirming that CeO₂ NRs maintain the rod structure after high temperature treatment. The EDX mapping show

that O and Ce are homogeneously distributed throughout the bulk of the CeO₂ NRs in CeO₂NRs/45Al₂O₃ (Figure 5c and 5d) and CeO₂NRs/45Al₂O₃_HT (Figure 5g and 5h). In contrast, Al does exist and is located at the external surface of the CeO₂ NRs (Figure 5b and 5f), on the top ~ 1 nm region, which is much thinner than a 4 – 5 nm shell what would be expected for 45 cycles ALD Al₂O₃ on the metal-OH surface.^{36, 38} In addition, the presence of Al is not continuous and conformal. These results suggest a different reaction mechanism than that in the common scheme of Al₂O₃ ALD. Based on the comparison between Figure 5b and 5f, HT treatment did not drive significant diffusion of Al into the bulk of CeO₂ NRs. It makes sense as Al-O bonds are stable at 700 °C. According to the overall EDX mapping of the CeO₂NRs/45Al₂O₃ and CeO₂NRs/45Al₂O₃_HT, Al distributes on all nanorods (Figure S2).

As ALD Al₂O₃ growth on CeO₂NRs at 200 °C does not follow the common nucleation and growth scheme on -OH surface, a different reaction mechanism happens. It was reported that –OH species on CeO₂ can be almost completely removed at 200 °C, which is same as our ALD treatment temperature (experimental section).^{39, 40} Therefore, we hypothesize that ALD Al₂O₃ does not nucleate on –OHs, which were removed by heating at 200 °C before ALD. To test our hypothesis, the same ALD sequence was applied onto the CeO₂ NRs at two different temperatures: 75 °C and 200 °C using the flat boat method (see in the experiment section). Figure 6 (a) and (b) show the TEM results of the CeO₂NRs/45Al₂O₃ and CeO₂NRs/45Al₂O₃(75 °C). At 200 °C, no visible Al₂O₃ shell was formed on the CeO₂NRs after 45 cycles of Al₂O₃ ALD (Figure 6a). At 75 °C, in contrast, an Al₂O₃ shell of ~4.5 nm thickness was formed over the CeO₂ NRs (Figure 6b). This result aligns with hypothesis. At 75 °C, the surface of CeO₂ NRs is populated with –OH groups, which promote the nucleation and growth of an Al₂O₃ shell through the common binary Al₂O₃ ALD chemistry. In addition, CeO₂NRs/14Al₂O₃(75 °C) (Figure S3) lose all low temperature srOSC in comparison to that of CeO₂NRs/45Al₂O₃, which is treated by ALD at 200 °C. It suggests that 14 cycles ALD Al₂O₃ at 75 °C deactivate or block all surface oxygen species. Such effect is consistent with the conformal Al₂O₃ coating from common ligand exchange reaction

between TMA and surface -OH group to form conformal an Al_2O_3 shell. At 200 °C, however, because a significant amount of -OH groups on CeO_2 surface were removed, TMA directly reacts with CeO_2 through a reaction mechanism that is different and slower than common binary Al_2O_3 ALD chemistry.

As shown in Figure 6c, heating CeO_2 NRs in N_2 at 200 °C significantly reduces the density of -OH groups. For instance, heating at 200 °C significantly reduces the broad peak centered at $\sim 3200\text{ cm}^{-1}$ and the peak centered at 1660 cm^{-1} in comparison with those from the sample at 75 °C. These two peaks are from hydrogen bonded OH groups. Hydrogen bonded OH groups exist due to the close approximation of OH groups, indicating high density of -OH groups. Heating at 200 °C reduces significantly larger portion of H bonded OH groups than heating at 75 °C as evidenced by the much larger negative peaks at 3200 and 1660 cm^{-1} than those from heating at 75 °C. The magnitude of reduction of these two peaks suggests that significant amount of OH groups on CeO_2 NRs have been removed at 200 °C in N_2 . Along with the decrease of these two peaks, heating at 75 and 200 °C increases the number of isolated -OH groups, as shown by the peaks 3702 , 3643 , and 3536 cm^{-1} .⁴¹⁻⁴³ These three peaks are corresponding to mono-coordinated OH, bridge OH, and triple bridge OH, whose structures are shown by OH(I), OH(II), and OH(III) in Figure 6d correspondingly. The presence of isolated -OH groups is due to the long distances between these -OH groups. Heating at 200 °C generates more isolated OH groups than that generated at 75 °C as shown by the larger positive isolated -OH IR peaks. The increase of these three peaks again indicates that the lower population of OH. This result is consistent with other reports.^{40, 41}

Figure 7a and 7b show the deconvoluted Ce 3d XPS spectrum of CeO_2NRs and $\text{CeO}_2\text{NRs}/45\text{Al}_2\text{O}_3$, respectively. Ce 3d shows split peaks resulting from the different valence states of Ce, including Ce^{3+} and Ce^{4+} .⁴⁴⁻⁴⁹ The $\text{Ce}^{4+}/3d_{3/2}$ and $\text{Ce}^{4+}/3d_{5/2}$ peaks centered at 916.9 eV and $899.1\text{ eV} \pm 0.2\text{ eV}$, respectively. The $\text{Ce}^{3+}/3d_{3/2}$ and $\text{Ce}^{3+}/3d_{5/2}$ peaks centered at 901.7 eV and $886.7\text{ eV} \pm 0.2\text{ eV}$, respectively.⁴⁴⁻⁴⁹ Other small satellite peaks are due to the energy-

gain processes, so-called shake-down peaks.^{45, 50} The concentration of Ce^{3+} increases from 0.266 at.% (CeO_2NRs) to 0.298 ($\text{CeO}_2\text{NRs}/45\text{Al}_2\text{O}_3$) based on the quantification of the corresponding Ce 3d XPS peaks. The higher concentration of Ce^{3+} indicates that ALD Al_2O_3 treatment reduces CeO_2 NRs to generate O vacancies and/or mobile oxygen species on the CeO_2 NRs surface. It is likely that Al^{3+} substitutes Ce ions during the ALD treatment. In addition, according to the inset photos of these two samples, $\text{CeO}_2\text{NRs}/45\text{Al}_2\text{O}_3$ is darker than CeO_2NRs . The darker color is a sign of partial reduction of CeO_2 .^{51, 52}

XRD spectra of CeO_2NRs and $\text{CeO}_2\text{NRs}/45\text{Al}_2\text{O}_3$ are presented in Figure 8. Both samples have the characteristic XRD peaks of CeO_2 , including {111}, {200}, {220}, and {311}. These peaks in $\text{CeO}_2\text{NRs}/45\text{Al}_2\text{O}_3$ shift to higher values than that of CeO_2 NRs. The calculated lattice constant of CeO_2 NRs is $5.415 \text{ \AA} \pm 0.0026 \text{ \AA}$, which decreased to $5.408 \text{ \AA} \pm 0.0019 \text{ \AA}$ after the ALD Al_2O_3 treatment. The shift of 2θ aligns with metal ion substituted CeO_2 ,^{53, 54} suggesting that Al ions substituted Ce ions to form Ce-Al-O_x lattices.

For the above-discussed H_2 -TPR test, ALD were carried onto CeO_2 NRs with the tubing method, in which the powder bed of CeO_2 NRs is $\sim 3 \text{ mm}$ in thickness. Because these CeO_2 NRs are nanosized objects, ALD reactants diffuse through torturous channels of nanometers in diameter inside the powder bed. So, the thickness of CeO_2 NRs powder bed could affect the concentration profile of ALD reactants in the bed.⁵⁵ We then tried the same ALD exposure scheme (5 min exposure for TMA per cycle) on CeO_2 NRs powder bed of $\sim 0.3 \text{ mm}$ in thickness (so called flatboat method). The srOSC of $\text{CeO}_2\text{NRs}(0.3\text{mm})/45\text{Al}_2\text{O}_3$ (0.3 mm is the thickness of the powder bed) is different than that produced from $\text{CeO}_2\text{NRs}/45\text{Al}_2\text{O}_3$ as shown by their TPR curves in Figure 9. $\text{CeO}_2\text{NRs}(0.3\text{mm})/45\text{Al}_2\text{O}_3$ lost most of its surface srOSC before HT. After HT treatment, the srOSC increases a little bit, potentially due to the change of the nanorod's surface during the HT. The srOSC of the sample is much smaller than that of $\text{CeO}_2\text{NRs}/45\text{Al}_2\text{O}_3\text{_{HT}}$ made by the tubing method. Therefore, the thickness of CeO_2 NRs powder bed affects the ALD reactions. According to the diffusion theory,⁵⁵ the time for TMA to diffuse through the sample bed could be

proportional to the th^2 (th : thickness of CeO_2 NRs powder bed), so the time needed for TMA to diffuse through the sample bed is 100 times in the tubing method. Through the coupled diffusion/reaction process, CeO_2 NRs react with TMA in a much smaller average rate in 3 mm-thick sample than 0.3 mm-thick sample. We hypothesize that the overall reaction time between ALD reactants and CeO_2 NRs needed to be reduced for 0.3 mm-thick bed in order to have the similar average extent of reaction as the 3 mm-thick bed. To prove this hypothesis, we used short exposure (SE) of ALD reactants, i.e., 30 s and 2 s exposure time for TMA and water in each ALD cycle for 0.3 mm-thick sample. The resulting TPR result of the $\text{CeO}_2\text{NRs}(0.3\text{mm})/45\text{Al}_2\text{O}_3(\text{SE})_{\text{HT}}$ is similar as that of $\text{CeO}_2\text{NRs}/45\text{Al}_2\text{O}_3_{\text{HT}}$, except a slightly lower surface reduction peak at $\sim 480^\circ\text{C}$ and better light-off temperature. Therefore, long reaction time (e.g., 5 min TMA exposure for 0.3 mm bed thickness) can eliminate the srOSC of CeO_2 NRs but short reaction time (e.g., 30 s TMA exposure) can enhance the srOSC. This result indicates that extent of reactions in ALD Al_2O_3 on the CeO_2 NRs is controllable by reaction time.

DISCUSSION

Based on the TEM (Figure 1) and TPR measurements (Figure 4), ALD Al_2O_3 treatment not only stabilizes the morphology of the CeO_2 NRs, but also increases their srOSC (from 25 °C to 700 °C). This new type of $\text{CeO}_2\text{NRs}/\text{Al}_2\text{O}_3$ can be applied in applications that operate at the temperatures 700 °C or higher and require a high srOSC below 500 °C, such as three-way catalysts or medium-temperature fuel cells. In this section, we present our hypothetical mechanisms underlying the improved thermal stability of morphology and srOSC of $\text{CeO}_2\text{NRs}/45\text{Al}_2\text{O}_3$ and the formation mechanism of $\text{CeO}_2\text{NRs}/45\text{Al}_2\text{O}_3$.

Why does $\text{CeO}_2\text{NRs}/45\text{Al}_2\text{O}_3$ maintain the nanorod morphology to 700 °C?

To answer this question, let's first exam why CeO_2 NRs deform into CeO_2 nanoparticles when they are annealed at 400 °C or above (Figure 1).^{15, 23, 25-27} This deformation is driven by the minimization of the molar Gibbs energy of the material at the same temperature and pressure (1 atmospheric pressure). *First*, the deformation reduces the specific surface area, thereby the specific surface Gibbs energy of the materials, because the CeO_2 NRs have a higher specific surface area than the deformed CeO_2 nanoparticles. *Second*, the deformed CeO_2 nanoparticles have a lower surface energy per cm^2 than that of the original CeO_2 NRs because CeO_2 NRs is dominated with surface facets of $\{110\}$ and $\{100\}$, which have higher surface energy than the dominating surface facets of $\{111\}$ on deformed CeO_2 nanoparticles.^{12, 19-21} Therefore, thermodynamically, annealing reduces the specific surface energy of CeO_2 .

Kinetically, CeO_2 NRs deform into nanoparticles because Ce ion moves around faster at higher temperatures. At 400 °C or above, Ce ions on surfaces acquire enough energy to break surface bonds and move around. Ce ions inside of CeO_2 lattice may move as well, but at a much slower rate, because atoms inside CeO_2 crystals form more bonds with surrounding atoms and need a higher energy to break more bonds in order to diffuse. The migration of Ce ions is accelerated at higher temperatures; therefore CeO_2 NRs deforms much faster at 700 °C than at 400 °C. The migration of O ions does not cause the deformation of CeO_2 NRs. For example,

during the reduction and oxidation of CeO₂ NRs at 400 °C (reduction at 400 °C in Figure 4a), O ions diffuse in and out of CeO₂ without deforming the crystal lattice. The reversible oxygen diffusion plays a key role to produce the srOSC of CeO₂.^{1, 56} Therefore, deformation of CeO₂ NRs is driven by the movement of Ce ions to reduce the material's Gibbs energy.

The migration of surface Ce ions is dramatically reduced in CeO₂NRs/45Al₂O₃ than in CeO₂ NRs because the superior thermal stability of CeO₂NRs/45Al₂O₃. We hypothesize that the decorated AlO_x species play two roles in improving the shape stability of CeO₂ NRs. *First*, the decorated AlO_x species physically block or slow down the surface diffusion of Ce ions. It is known that the surface diffusion of atoms can be dramatically reduced by even an atomic step. *Second*, doped Al³⁺ will block the hop of Ce ions because doped Al³⁺ ions will not migrate as Al-O bonding is hard to break (evidenced by the absence of oxygen storage capacity of Al₂O₃) and these doped Al³⁺ reduces the number of vacancies that Ce ions can hop through.

Why does CeO₂NRs/45Al₂O₃ has a much larger srOSC than that of pure CeO₂ NRs?

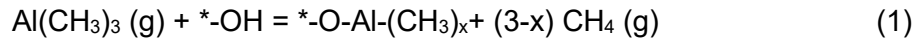
The following two mechanisms contribute to the much larger srOSC of CeO₂NRs/45Al₂O₃ upto 700°C. *First*, majority of reducible surface oxygen from Ce-O bonding are still available (peak centers at 480 °C in Figure 4) because Al₂O₃ ALD does not form a conformal coverage around CeO₂ due to the sluggish nucleation and growth kinetics of Al₂O₃ ALD on CeO₂ at 200 °C (Figure 6). This non-conformal coverage of Al₂O₃ is evidenced by the HAADF-EDX analyses (Figure 5).

Second, new types of reducible Ce species emerge as shown by the new reduction between 500 to 600 °C (Figure 4). Based on the experimental data and the literature reports,^{8, 54, 57, 58} we hypothesized the higher srOSC is from the formation of reducible Al-O-Ce-**O**- species on the surface and the sub-surfaces of CeO₂ NRs. Although oxygen in Al-O cannot be reduced at 700 °C, oxygen that bonds to Ce in -Al-O-Ce-**O**- but is not shared with Al could be activated at a lower temperature than oxygen in bulk CeO₂ lattice. Such -Al-O-Ce-**O**- species can be formed by substituting Ce⁴⁺ (radius of 1.01 Å) with the smaller Al³⁺ ions (radius of 0.53 Å). In -Al-O-Ce-**O**-, the Al³⁺ ion will draw the oxygen ion between Al and Ce closer to Al. The substitution is confirmed

by formation of Ce^{3+} and color change (Figure 7). The simulated lattice constant of Al-O-Ce-O- is $\sim 3.772 \text{ \AA}$,⁵⁹ which is smaller than the lattice constant of CeO_2 (5.415 \AA). This smaller lattice constant agrees with the XRD measurements (Figure 8), which shows that the lattice constant of $\text{CeO}_2\text{NRs}/45\text{Al}_2\text{O}_3$ is smaller than that of CeO_2 NRs.^{53, 54} In addition, DFT calculations show that the metal ion doped CeO_2 has longer Ce-O bond, which is weaker than the original bond.⁴³ The formation of Al-O-Ce-O- is consistent with findings in literature reports,^{8, 54, 57, 58} which show that thermal stability and srOSC of non-shape engineered CeO_2 can be enhanced by doping with metal ions (M), such as La^{3+} , Zr^{4+} , Ti^{4+} , Sn^{4+} etc. Therefore, new -Al-O-Ce-O- species are formed in $\text{CeO}_2\text{NRs}/45\text{Al}_2\text{O}_3$ and are reducible at $500 - 600^\circ\text{C}$.^{53, 60-64} These -Al-O-Ce-O- clusters sit in different configurations and environments to produce a wide oxygen reduction peak (Figure 4b).

How does ALD nucleate on CeO_2 NRs?

Our experiment results (Figure 1, 2, 5 and 6) show that Al_2O_3 ALD nucleates differently on -OH free CeO_2 NRs than on -OH dominated impermeable substrates. As shown in Figure 1, 2, 5, and 6a, $\text{CeO}_2\text{NRs}/45\text{Al}_2\text{O}_3$ does not have a conformal 4-5 nm Al_2O_3 -shell, which is expected for steady state 45 cycles of Al_2O_3 ALD on surface covered by -OHs (Figure 6b and other reports^{55, 65}). The simplified reaction mechanism of TMA with -OH surface sites is shown in Eq. 1, where g represents vapor and * represents the surface.



However, a significant amount of surface OH groups are removed from CeO_2 NRs at 200°C ,^{39, 40} as evidenced by the DRIFTS results (Figure 6c). TMA will compete aggressively with Ce for oxygen because TMA is one of the strongest Lewis acids, meaning the Al atom will like to bond with a lone pair of electrons on O. This reaction will reduce Ce^{4+} to Ce^{3+} and create oxygen vacancies for Ce. The XPS analysis (Figure 7) shows that concentration of Ce^{3+} increases after the ALD Al_2O_3 treatment. Meanwhile, Al^{3+} cations from ALD Al_2O_3 will dope into the lattice of CeO_2 NRs to form Al-O-Ce-O- on the surface and subsurface. XRD (Figure 8) confirms Al doping. -CH₃ ligands on TMA could be oxidized into carbonyl groups or CO_2 , or bond with Ce ion to form volatile

species. When adsorbed on CeO_2 that is reduced TMA, H_2O can reoxidize the reduced CeO_2 with H_2 evolution.^{66, 67} The reoxidation by H_2O coupled with dihydroxylation by heating will supply CeO_2 with oxygen instead of $-\text{OH}$ groups for the reaction with the next exposure of TMA. The reaction between TMA and CeO_2 at 200°C produces slow nucleation of ALD Al_2O_3 , which is consistent with results from Figure 9. If the reaction time is short, the reaction produces Al doped CeO_2 , such as $\text{CeO}_2\text{NRs}/45\text{Al}_2\text{O}_3$ and $\text{CeO}_2\text{NRs}(0.3\text{mm})/45\text{Al}_2\text{O}_3(\text{SE})$ which creates more reducible oxygen species on the surface and sub-surfaces, therefore increases the srOSC of the NRs (Figure 9). If the reaction time is too long, the Al doped CeO_2 will be convert into CeAlO_3 , which eliminate the amount of the reducible oxygen species on the surface and subsurface.

CONCLUSIONS

We presented a controllable post-synthesis Al doping method, *i. e.*, ALD Al_2O_3 at 200°C , to not only sustain the morphology of CeO_2 NRs at high temperatures but also enhance their thermal stability and srOSC. Although SENs could been applied in a range of fields, including catalysis, photonics, optoelectronics, surface enhanced Raman scattering, and environmental issue, they often suffer from poor thermal stability. Our low temperature chemical doping concept could be adopted to improve thermal stability of other SENs while maintain or even enhance their unique functionalities.

METHODS

Preparation of CeO₂ nanorods.

The CeO₂ nanorods were synthesized through a hydrothermal method. Briefly, 8 ml of 6 M NaOH aqueous solution were added into 0.1 M Ce(NO₃)₃·6H₂O (Acros Organics 99.5%). This mixture was stirred for about 15 s in a Teflon bottle (200 mL). The Teflon bottle was loaded into a autoclave, which was then tightly sealed and transferred into a programmable box furnace. The hydrothermal reaction procedure was carried out at 90 °C for 48 hrs to produce CeO₂ NRs. After the autoclave was cooled down to room temperature, the precipitates were collected and then washed with deionized water and ethanol. The as-prepared samples were obtained by drying in air at 60 °C overnight.

ALD Chemical and materials.

ALD precursors were trimethyl aluminum (TMA) (98%, Strem Chemicals) and deionized water (DI H₂O) (18 MΩ, water filtration system from Thermo Fisher Scientific LLC). The carrier and purging gas for the ALD process is ultrahigh purity N₂ (99.999%, Airgas). Isopropyl alcohol (IPA) (99.5% BDH) was used to clean the sample holder.

ALD sample holder cleaning. Sample holders used in the ALD process include ceramic boat and quartz tube were cleaned by 30 min sonication (Branson 5510) in DI water and IPA, respectively, and dried on the hotplate at 400 °C for 1 hour. The metal wire cloth (Gerard Daniel Worldwide) covered on the ceramic boat was cleaned by the same procedure.

ALD processes

ALD on 3 mm thick of CeO₂ NRs powder bed (tube method). A quartz tube with diameter of 10 mm was used as the ALD sample holder for CeO₂ nanorods (Figure S4). CeO₂ nanorods were loaded into the quartz tube with one side blocked by the quartz wool, another side of the tube was also blocked by the quartz after the sample loading. The average CeO₂ nanorod bed thickness in the quartz tube was 3 mm. Due to the difficulty of the gas diffusion into the closed packed nanorod

sample bed, long exposure time was used for the precursors. The ALD temperature was 200 °C. In each ALD cycle, the ALD sequence was: pre-purge the sample for 20 mins; pumping down the system to 10^{-2} torr; shut down the pump; TMA pulsing for 8 s (~ 2 torr); TMA exposure for 5 min; pump out TMA until system is 10^{-2} torr; N₂ purging for 120 s; H₂O dose for 20 s with carrier gas flow; N₂ purging for 120 s. Repeat the sequence for another layer of coating. To loosen the powder bed, the chamber was continuously vibrated by a homemade vibrator during the ALD process.

ALD on 0.3mm thick of CeO₂ NRs powder bed (flatbed method). A ceramic boat with flat bottom was used as the ALD sample holder for CeO₂ nanorods (Figure S3). Nanorods powder were loaded into the boat and shook into a thin film which uniformly cover the bottom of the boat. The powder bed thickness is ~ 0.3 mm. ALD chamber was at 200 °C. The ALD sequence was: pre-purge the sample for 20 mins; pumping down the system to 10^{-2} torr; shut down the pump; TMA pulsing for 8 s (~ 2 torr); TMA exposure for 5 min; pump out TMA until system is 10^{-2} torr; N₂ purging for 120 s; H₂O dose for 20 s with carrier gas flow; N₂ purging for 120 s. To check the effect of exposure time of TMA and H₂O on the reaction, we also used 30 s and 2s as the exposure time for TMA and the H₂O, respectively, with other experiment conditions and ALD sequences were kept the same.

Heat treatment (HT). Samples were loaded into a quartz boat and annealed inside the heat furnace (Lindberg/Blue M, ThermoFisher) at 700 °C for 5 hours in air. The ramping rate of the temperature was 10 °C/min.

Characterizations

TEM. FEI Tecnai F-20 was used to characterize the morphology of CeO₂ nanorods before and after various treatments. Nanorod powders were dispersed into methanol by sonication and the solution was drop casted onto copper TEM grids (Supported carbon film, 200 mesh, TED PELLA).

STEM. Electron microscopy was carried out using Hitachi HF3300 high-resolution TEM-STEM at 300 kV and Nion UltraSTEM 200 at 200 kV. EDX mapping was carried out using FEI Talos microscope at 200 kV.

TPR. Hydrogen temperature programmed reduction (H_2 -TPR) was performed using a Micrometrics AutoChemTM II 2920 with the temperature rising from ambient temperature to 700 °C at a rate of 10 °C/min. 50 mL/min of steam (5% H_2 and 95% Ar) is passed through the testing powder samples (~100 mg), which is loaded in a quartz U-type reactor. H_2 -TPR cycling experiments were performed 10 times in the same experimental apparatus. Between each H_2 -TPR cycle, the quartz U-type reactor was taken down from the instrument, and the powder sample was exposed to air for 24 h to replenish the oxygen.

Diffuse Reflectance Infrared Fourier Transform Spectroscopy (DRIFTS). PIKE Technologies DiffusIR was used to study the change of –OH groups on CeO_2 nanorods at different temperatures in N_2 . CeO_2 nanorods was added into the Al_2O_3 crucibles for the DRIFTS measurement. The DRIFTS chamber was continuously purged by N_2 . The IR spectra were taken, respectively, after CeO_2 nanorods were heated to 75 °C and 200 °C and maintained at the temperature for 20 mins. The resulting spectra of CeO_2 NRs at 75 °C and 200 °C was obtained by using the spectrum of CeO_2 nanorods at 25 °C as the reference.

Acknowledgement

PENG thanks the Donors of the American Chemical Society Petroleum Research Fund (#56265-DNI10) for supporting this research. WANG thanks the financial support from the National Science Foundation (NSF CHE-1657943 and NSF CBET-1856729). Electron microscopy at ORNL (S.Z.Y.) was supported by the U.S. Department of Energy, Office of Science, Basic Energy Sciences, Materials Sciences and Engineering Division and performed in part as a user proposal at the ORNL Center for Nanophase Materials Sciences, which is a DOE Office of the Science

User Facilities. This research used resources of the Center for Functional Nanomaterials, which is a U.S. DOE Office of Science Facility, at Brookhaven National Laboratory under Contract No. DE-SC0012704.

REFERENCES AND NOTES

1. Montini, T.; Melchionna, M.; Monai, M.; Fornasiero, P., Fundamentals and Catalytic Applications of CeO₂-Based Materials. *Chem Rev* **2016**, *116* (10), 5987-6041.
2. Vogt, E. T. C.; Weckhuysen, B. M., Fluid catalytic cracking: recent developments on the grand old lady of zeolite catalysis. *Chemical Society Reviews* **2015**, *44* (20), 7342-7370.
3. Fino, D.; Bensaid, S.; Piumetti, M.; Russo, N., A Review on the Catalytic Combustion of Soot in Diesel Particulate Filters for Automotive Applications: From Powder Catalysts to Structured Reactors. *Applied Catalysis A-General* **2016**, *509*, 75-96.
4. Murray, E. P.; Tsai, T.; Barnett, S. A., A Direct-Methane Fuel Cell with a Ceria-Based Anode. *Nature* **1999**, *400* (6745), 649-651.
5. Desaunay, T.; Bonura, G.; Chiodo, V.; Freni, S.; Couzinie, J. P.; Bourgon, J.; Ringuède, A.; Labat, F.; Adamo, C.; Cassir, M., Surface-dependent oxidation of H₂ on CeO₂ surfaces. *J. Catal.* **2013**, *297*, 193-201.
6. Yao, H. C.; Yao, Y. F. Y., Ceria in Automotive Exhaust Catalysts .1. Oxygen Storage. *J. Catal.* **1984**, *86* (2), 254-265.
7. Shyu, J. Z.; Weber, W. H.; Gandhi, H. S., Surface Characterization of Alumina-Supported Ceria. *J. Phys. Chem.* **1988**, *92* (17), 4964-4970.
8. Fornasiero, P.; Balducci, G.; DiMonte, R.; Kaspar, J.; Sergo, V.; Gubitosa, G.; Ferrero, A.; Graziani, M., Modification of the Redox Behaviour of CeO₂ Induced by Structural Doping with ZrO₂. *J. Catal.* **1996**, *164* (1), 173-183.
9. Vlaic, G.; Fornasiero, P.; Geremia, S.; Kaspar, J.; Graziani, M., Relationship between the Zirconia-Promoted Reduction in the RH-Loaded Ce_{0.5}Zr_{0.5}O₂ Mixed Oxide and the Zr-O Local Structure. *J. Catal.* **1997**, *168* (2), 386-392.
10. Trovarelli, A.; de Leitenburg, C.; Boaro, M.; Dolcetti, G., The utilization of ceria in industrial catalysis. *Catal. Today* **1999**, *50* (2), 353-367.

11. He, J. J.; Wang, C. X.; Zheng, T. T.; Zhao, Y. K., Thermally Induced Deactivation and the Corresponding Strategies for Improving Durability in Automotive Three-Way Catalysts. *Johnson Matthey Tech* **2016**, *60* (3), 196-203.
12. Zhou, K. B.; Wang, X.; Sun, X. M.; Peng, Q.; Li, Y. D., Enhanced Catalytic Activity of Ceria Nanorods from Well-Defined Reactive Crystal Planes. *J. Catal.* **2005**, *229* (1), 206-212.
13. Liu, X. W.; Zhou, K. B.; Wang, L.; Wang, B. Y.; Li, Y. D., Oxygen Vacancy Clusters Promoting Reducibility and Activity of Ceria Nanorods. *J. Am. Chem. Soc.* **2009**, *131* (9), 3140-3141.
14. Ta, N.; Liu, J. Y.; Chenna, S.; Crozier, P. A.; Li, Y.; Chen, A. L.; Shen, W. J., Stabilized Gold Nanoparticles on Ceria Nanorods by Strong Interfacial Anchoring. *J. Am. Chem. Soc.* **2012**, *134* (51), 20585-20588.
15. Wu, Z. L.; Li, M. J.; Howe, J.; Meyer, H. M.; Overbury, S. H., Probing Defect Sites on CeO₂ Nanocrystals with Well-Defined Surface Planes by Raman Spectroscopy and O₂ Adsorption. *Langmuir* **2010**, *26* (21), 16595-16606.
16. Wu, Z. L.; Li, M. J.; Overbury, S. H., On the Structure Dependence of CO Oxidation over CeO₂ Nanocrystals with Well-Defined Surface Planes. *J. Catal.* **2012**, *285* (1), 61-73.
17. Wu, Z. L.; Li, M. J.; Mullins, D. R.; Overbury, S. H., Probing the Surface Sites of CeO₂ Nanocrystals with Well-Defined Surface Planes via Methanol Adsorption and Desorption. *ACS Catalysis* **2012**, *2* (11), 2224-2234.
18. Tong, X. F.; Luo, T.; Meng, X.; Wu, H.; Li, J. L.; Liu, X. J.; Ji, X. N.; Wang, J. Q.; Chen, C. S.; Zhan, Z. L., Shape-Dependent Activity of Ceria for Hydrogen Electro-Oxidation in Reduced-Temperature Solid Oxide Fuel Cells. *Small* **2015**, *11* (41), 5581-5588.
19. Mai, H. X.; Sun, L. D.; Zhang, Y. W.; Si, R.; Feng, W.; Zhang, H. P.; Liu, H. C.; Yan, C. H., Shape-Selective Synthesis and Oxygen Storage Behavior of Ceria Nanopolyhedra, Nanorods, and Nanocubes. *J. Phys. Chem. B* **2005**, *109* (51), 24380-24385.

20. Baudin, M.; Wojcik, M.; Hermansson, K., Dynamics, Structure and Energetics of the (111), (011) and (001) Surfaces of Ceria. *Surf. Sci.* **2000**, *468* (1-3), 51-61.
21. Nolan, M.; Grigoleit, S.; Sayle, D. C.; Parker, S. C.; Watson, G. W., Density functional theory studies of the structure and electronic structure of pure and defective low index surfaces of ceria. *Surf. Sci.* **2005**, *576* (1-3), 217-229.
22. Trovarelli, A.; Llorca, J., Ceria Catalysts at Nanoscale: How Do Crystal Shapes Shape Catalysis? *Acs Catalysis* **2017**, *7* (7), 4716-4735.
23. Aneggi, E.; Wiaterski, D.; de Leitenburg, C.; Llorca, J.; Trovarelli, A., Shape-Dependent Activity of Ceria in Soot Combustion. *Acs Catalysis* **2014**, *4* (1), 172-181.
24. Esch, F.; Fabris, S.; Zhou, L.; Montini, T.; Africh, C.; Fornasiero, P.; Comelli, G.; Rosei, R., Electron Localization Determines Defect Formation on Ceria Substrates. *Science* **2005**, *309* (5735), 752-755.
25. Jones, J.; Xiong, H. F.; Delariva, A. T.; Peterson, E. J.; Pham, H.; Challa, S. R.; Qi, G. S.; Oh, S.; Wiebenga, M. H.; Hernandez, X. I. P.; Wang, Y.; Datye, A. K., Thermally Stable Single-Atom Platinum-on-Ceria Catalysts via Atom Trapping. *Science* **2016**, *353* (6295), 150-154.
26. Zhu, S. H.; Lian, X. Y.; Fan, T. T.; Chen, Z.; Dong, Y. Y.; Weng, W. Z.; Yi, X. D.; Fang, W. P., Thermally stable core-shell Ni/nanorod-CeO₂@SiO₂ catalyst for partial oxidation of methane at high temperatures. *Nanoscale* **2018**, *10* (29), 14031-14038.
27. Mock, S. A.; Sharp, S. E.; Stoner, T. R.; Radetic, M. J.; Zell, E. T.; Wang, R., CeO₂ nanorods-supported transition metal catalysts for CO oxidation. *Journal of colloid and interface science* **2016**, *466*, 261-267.
28. Forzatti, P.; Lietti, L., Catalyst deactivation. *Catal Today* **1999**, *52* (2-3), 165-181.
29. Zeng, P.; Zajac, S.; Clapp, P. C.; Rifkin, J. A., Nanoparticle sintering simulations. *Mat Sci Eng a-Struct* **1998**, *252* (2), 301-306.
30. Cao, A.; Lu, R.; Veser, G., Stabilizing metal nanoparticles for heterogeneous catalysis. *Phys Chem Chem Phys* **2010**, *12* (41), 13499-13510.

31. Shewmon, P., *Diffusion in solids*. Springer: 2016.
32. Resasco, J.; Dasgupta, N. P.; Rosell, J. R.; Guo, J. H.; Yang, P. D., Uniform Doping of Metal Oxide Nanowires Using Solid State Diffusion. *J. Am. Chem. Soc.* **2014**, *136* (29), 10521-10526.
33. Lu, J. L.; Fu, B. S.; Kung, M. C.; Xiao, G. M.; Elam, J. W.; Kung, H. H.; Stair, P. C., Coking- and Sintering-Resistant Palladium Catalysts Achieved Through Atomic Layer Deposition. *Science* **2012**, *335* (6073), 1205-1208.
34. McCarty, J. G.; Gusman, M.; Lowe, D.; Hildenbrand, D.; Lau, K., Stability of supported metal and supported metal oxide combustion catalysts. *Catal Today* **1999**, *47* (1-4), 5-17.
35. Bartholomew, C. H., Mechanisms of catalyst deactivation. *Applied Catalysis a-General* **2001**, *212* (1-2), 17-60.
36. Elam, J. W.; Groner, M. D.; George, S. M., Viscous Flow Reactor with Quartz Crystal Microbalance for Thin Film Growth by Atomic Layer Deposition. *Rev. Sci. Instrum.* **2002**, *73* (8), 2981-2987.
37. Lopez, J. M.; Gilbank, A. L.; Garcia, T.; Solsona, B.; Agouram, S.; Torrente-Murciano, L., The prevalence of surface oxygen vacancies over the mobility of bulk oxygen in nanostructured ceria for the total toluene oxidation. *Appl Catal B-Environ* **2015**, *174*, 403-412.
38. Groner, M.; Fabreguette, F.; Elam, J.; George, S., Low-temperature Al₂O₃ atomic layer deposition. *Chem Mater* **2004**, *16* (4), 639-645.
39. Plakhova, T. V.; Romanchuk, A. Y.; Butorin, S. M.; Konyukhova, A. D.; Egorov, A. V.; Shiryayev, A. A.; Baranchikov, A. E.; Dorovatovskii, P. V.; Huthwelker, T.; Gerber, E., Towards the surface hydroxyl species in CeO₂ nanoparticles. *Nanoscale* **2019**, *11* (39), 18142-18149.
40. Mullins, D. R.; Albrecht, P. M.; Chen, T. L.; Calaza, F. C.; Biegalski, M. D.; Christen, H. M.; Overbury, S. H., Water Dissociation on CeO₂(100) and CeO₂(111) Thin Films. *J. Phys. Chem. C* **2012**, *116* (36), 19419-19428.

41. Badri, A.; Binet, C.; Lavalley, J. C., An FTIR Study of Surface Ceria Hydroxy Groups During a Redox Process with H₂. *Journal of the Chemical Society-Faraday Transactions* **1996**, 92 (23), 4669-4673.
42. Binet, C.; Daturi, M.; Lavalley, J. C., IR Study of Polycrystalline Ceria Properties in Oxidised and Reduced States. *Catal. Today* **1999**, 50 (2), 207-225.
43. Tsyganenko, A. A.; Filimonov, V. N., Infrared-Spectra of Surface Hydroxyl Groups and Crystalline-Structure of Oxides. *Spectroscopy Letters* **1972**, 5 (12), 477-487.
44. Beche, E.; Charvin, P.; Perarnau, D.; Abanades, S.; Flamant, G., Ce 3d XPS investigation of cerium oxides and mixed cerium oxide (Ce_xTi_{1-x}O₂). *Surf Interface Anal* **2008**, 40 (3-4), 264-267.
45. Burroughs, P.; Hamnett, A.; Orchard, A. F.; Thornton, G., Satellite Structure in X-Ray Photoelectron-Spectra of Some Binary and Mixed Oxides of Lanthanum and Cerium. *J Chem Soc Dalton* **1976**, (17), 1686-1698.
46. Praline, G.; Koel, B. E.; Hance, R. L.; Lee, H. I.; White, J. M., X-Ray Photoelectron Study of the Reaction of Oxygen with Cerium. *J Electron Spectrosc* **1980**, 21 (1), 17-30.
47. Paparazzo, E.; Ingo, G. M.; Zacchetti, N., X-Ray-Induced Reduction Effects at CeO₂ Surfaces - an X-Ray Photoelectron-Spectroscopy Study. *J Vac Sci Technol A* **1991**, 9 (3), 1416-1420.
48. Romeo, M.; Bak, K.; Elfallah, J.; Lenormand, F.; Hilaire, L., Xps Study of the Reduction of Cerium Dioxide. *Surf Interface Anal* **1993**, 20 (6), 508-512.
49. Mullins, D. R.; Overbury, S. H.; Huntley, D. R., Electron spectroscopy of single crystal and polycrystalline cerium oxide surfaces. *Surf Sci* **1998**, 409 (2), 307-319.
50. Kotani, A.; Jo, T.; Parlebas, J. C., Many-Body Effects in Core-Level Spectroscopy of Rare-Earth Compounds. *Adv Phys* **1988**, 37 (1), 37-85.
51. Wang, R. G.; Dangerfield, R., Seed-Mediated Synthesis of Shape-Controlled CeO₂ Nanocrystals. *Rsc Advances* **2014**, 4 (7), 3615-3620.

52. Xu, C.; Qu, X., Cerium oxide nanoparticle: a remarkably versatile rare earth nanomaterial for biological applications. *NPG Asia Materials* **2014**, 6 (3), e90-e90.
53. Dutta, G.; Waghmare, U. V.; Baidya, T.; Hegde, M. S.; Priolkar, K. R.; Sarode, P. R., Reducibility of $\text{Ce}_{1-x}\text{Zr}_x\text{O}_2$: origin of enhanced oxygen storage capacity. *Catal Lett* **2006**, 108 (3-4), 165-172.
54. Hegde, M. S.; Beraba, P., Noble metal ion substituted CeO_2 catalysts: Electronic interaction between noble metal ions and CeO_2 lattice. *Catal Today* **2015**, 253, 40-50.
55. Elam, J. W.; Routkevitch, D.; Mardilovich, P. P.; George, S. M., Conformal Coating on Ultrahigh-Aspect-Ratio Nanopores of Anodic Alumina by Atomic Layer Deposition. *Chem. Mat.* **2003**, 15 (18), 3507-3517.
56. Reinhardt, K.; Winkler, H., Cerium mischmetal, cerium alloys, and cerium compounds. *Ullmann's encyclopedia of industrial chemistry* **2000**.
57. Wang, C.; Wen, C.; Lauterbach, J.; Sasmaz, E., Superior oxygen transfer ability of $\text{Pd/MnO}_x\text{-CeO}_2$ for enhanced low temperature CO oxidation activity. *Appl Catal B-Environ* **2017**, 206, 1-8.
58. Hou, X. L.; Lu, Q. Q.; Wang, X. C., Enhanced catalytic properties of La-doped CeO_2 nanopowders synthesized by hydrolyzing and oxidizing $\text{Ce}_{46}\text{La}_{54}\text{O}_{190}$ alloys. *J Sci* **2017**, 2 (1), 41-44.
59. Jiang, L. Q.; Guo, J. K.; Liu, H. B.; Zhu, M.; Zhou, X.; Wu, P.; Li, C. H., Prediction of lattice constant in cubic perovskites. *J Phys Chem Solids* **2006**, 67 (7), 1531-1536.
60. Gupta, A.; Hegde, M. S.; Priolkar, K. R.; Waghmare, U. V.; Sarode, P. R.; Emura, S., Structural Investigation of Activated Lattice Oxygen in $\text{Ce}_{1-x}\text{Sn}_x\text{O}_2$ and $\text{Ce}_{1-x-y}\text{Sn}_x\text{Pd}_y\text{O}_{2-\delta}$ by EXAFS and DFT calculation. *Chem Mater* **2009**, 21 (24), 5836-5847.
61. Gupta, A.; Kumar, A.; Waghmare, U. V.; Hegde, M. S., Origin of activation of Lattice Oxygen and Synergistic Interaction in Bimetal-Ionic $\text{Ce}_{0.89}\text{Fe}_{0.1}\text{Pd}_{0.01}\text{O}_{2-\delta}$ Catalyst. *Chem Mater* **2009**, 21 (20), 4880-4891.

62. Scanlon, D. O.; Morgan, B. J.; Watson, G. W., The origin of the enhanced oxygen storage capacity of $\text{Ce}_{1-x}(\text{Pd/Pt})_x\text{O}_2$. *Phys Chem Chem Phys* **2011**, *13* (10), 4279-4284.
63. Shapovalov, V.; Metiu, H., Catalysis by doped oxides: CO oxidation by $\text{AuCe}_{1-x}\text{O}_2$. *J Catal* **2007**, *245* (1), 205-214.
64. Yang, Z. X.; Luo, G. X.; Lu, Z. S.; Woo, T. K.; Hermansson, K., Structural and electronic properties of NM-doped ceria (NM = Pt, Rh): a first-principles study. *J Phys-Condens Mat* **2008**, *20* (3).
65. George, S. M., Atomic Layer Deposition: An Overview. *Chem. Rev.* **2010**, *110* (1), 111-131.
66. Otsuka, K.; Hatano, M.; Morikawa, A., Hydrogen from Water by Reduced Cerium Oxide. *J. Catal.* **1983**, *79* (2), 493-496.
67. Padeste, C.; Cant, N. W.; Trimm, D. L., The Influence of Water on the Reduction and Reoxidation of Ceria. *Catalysis Letters* **1993**, *18* (3), 305-316.

Figures

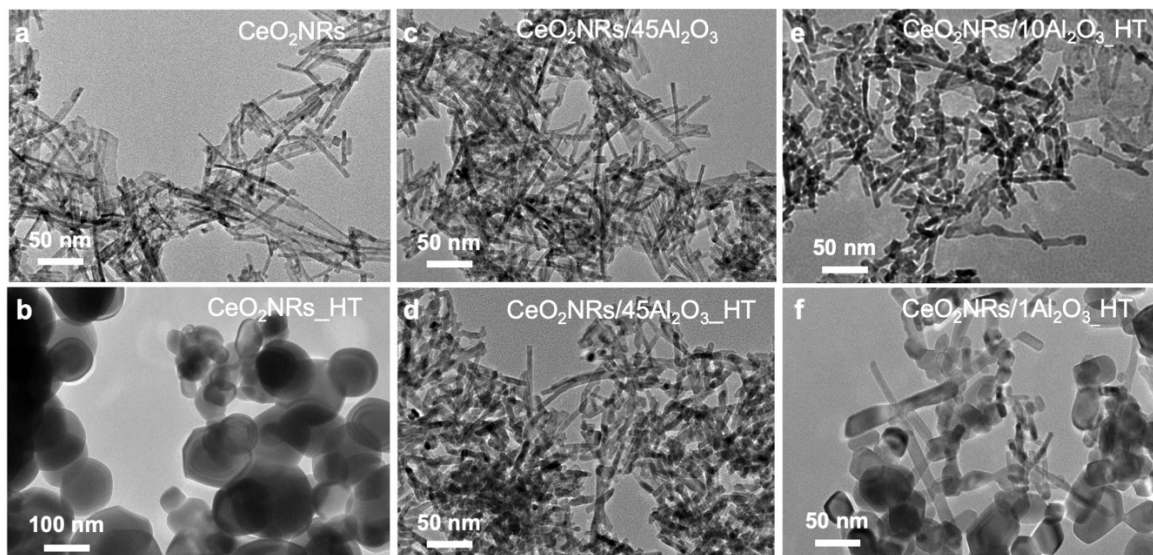


Figure 1. TEM images of (a) CeO₂ NRs; (b) CeO₂NRs_HT (CeO₂ NRs after HT); (c) CeO₂NRs/45Al₂O₃; (d) CeO₂NRs/45Al₂O₃_HT; (e) CeO₂NRs/15Al₂O₃_HT; (h) CeO₂NRs/1Al₂O₃_HT. CeO₂NRs/nAl₂O₃_HT: CeO₂ NRs with n cycles of Al₂O₃ ALD followed by HT. HT: heat treatment: 700 °C in N₂ for 5 h. ALD Al₂O₃ was carried at 200 °C with trimethyl aluminum [Al(CH₃)₃] & H₂O as the reactants.

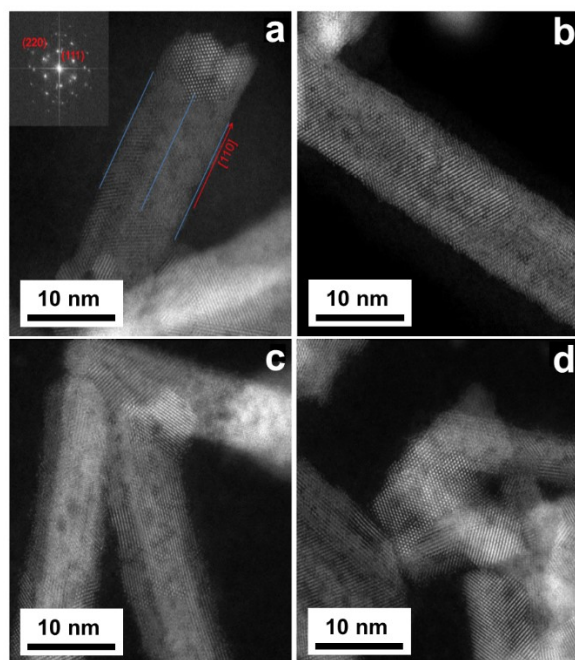


Figure 2. HRTEM of fresh CeO_2 NRs (**a** and **b**) and $\text{CeO}_2\text{NRs}/45\text{Al}_2\text{O}_3$ (**c** and **d**) before the thermal treatment. The inset figure in (a) shows the corresponding Fourier transform image of the CeO_2 NR. The arrow in (a) illustrates the [110] direction of CeO_2 NRs.

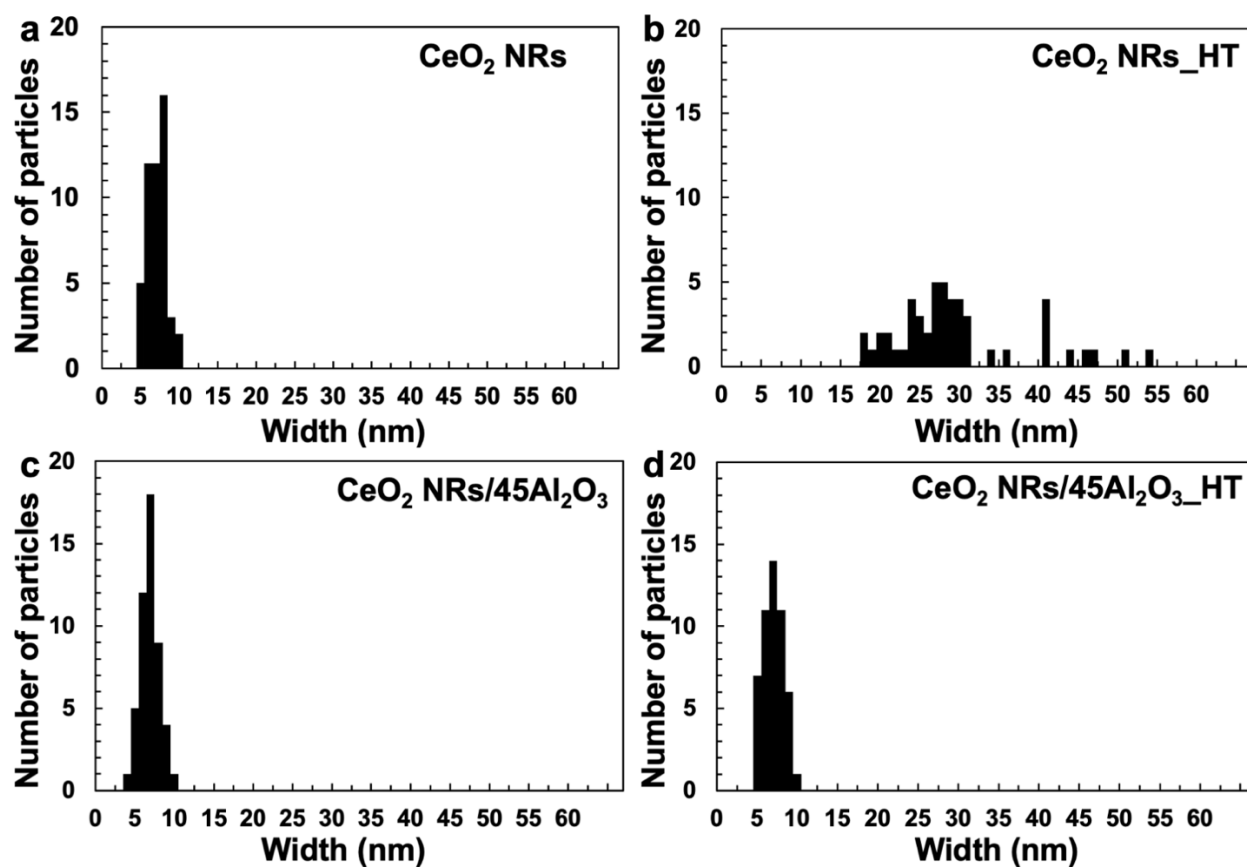


Figure 3. Size distribution of (a) CeO₂ NRs, (b) CeO₂NRs_HT; (c) CeO₂NRs/45Al₂O₃ (d) CeO₂ NRs/45Al₂O₃_HT. CeO₂ NRs deformed significantly by HT. CeO₂NRs/45Al₂O₃ maintained its nanorod shape after HT.

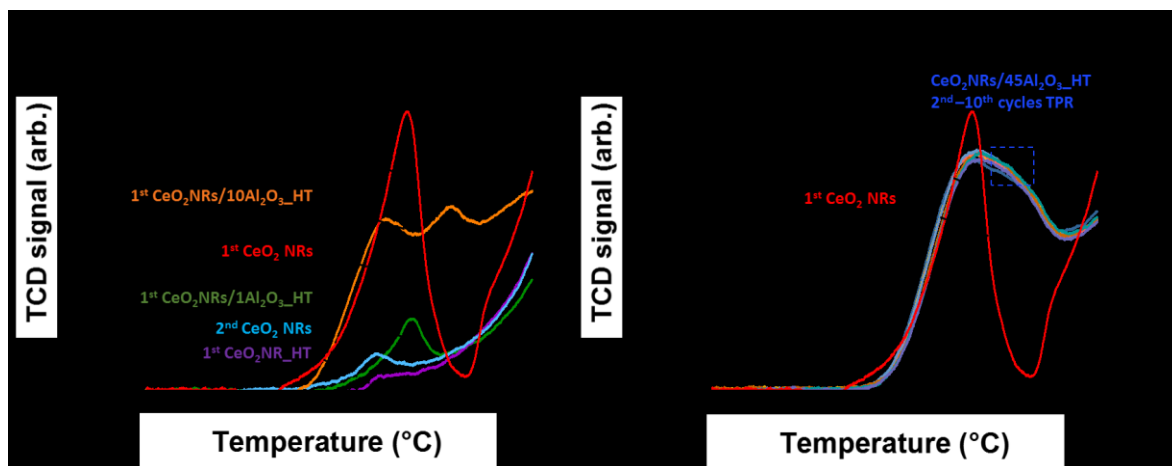


Figure 4. H₂ TPR profile of (a) CeO₂ NRs in 1st and 2nd cycles of TPR; CeO₂NRs_HT; CeO₂NRs/1Al₂O₃_HT; CeO₂NRs/10Al₂O₃_HT; CeO₂NRs/45Al₂O₃_HT for comparison; (b) CeO₂ NRs 1st cycle TPR; CeO₂NRs/45Al₂O₃_HT in the 1st – 10th cycles of TPR. The amount of H₂ uptake is normalized to the weight of the sample. The area underneath a curve is a measure of OSC of samples. The ALD Al₂O₃ treated samples should have larger peaks than that in the figure if we use the CeO₂ as the mass base. The low temperature peak (center at ~ 480 °C) is from surface oxygen. The reduction of bulk oxygen from CeO₂ NRs has a peak located at > 700 °C.

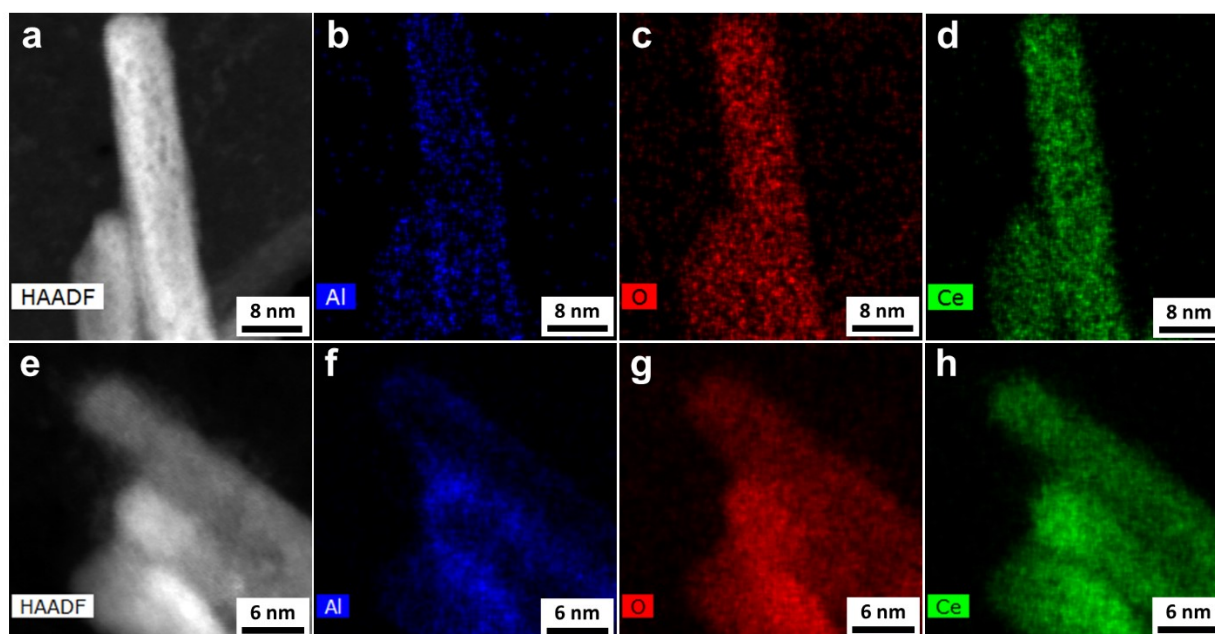


Figure 5. HAADF-STEM EDAX mapping of two selected $\text{CeO}_2\text{NRs}/45\text{Al}_2\text{O}_3$ samples, (a-d) sample 1 and (e-h) sample 2, including morphology (a and e), Al distribution (b and f), O distribution (c and g), and Ce distribution (d and h). Ce and O are uniformly distributed inside the nanorods. Al (b-f) is only on the surface of the nanorods.

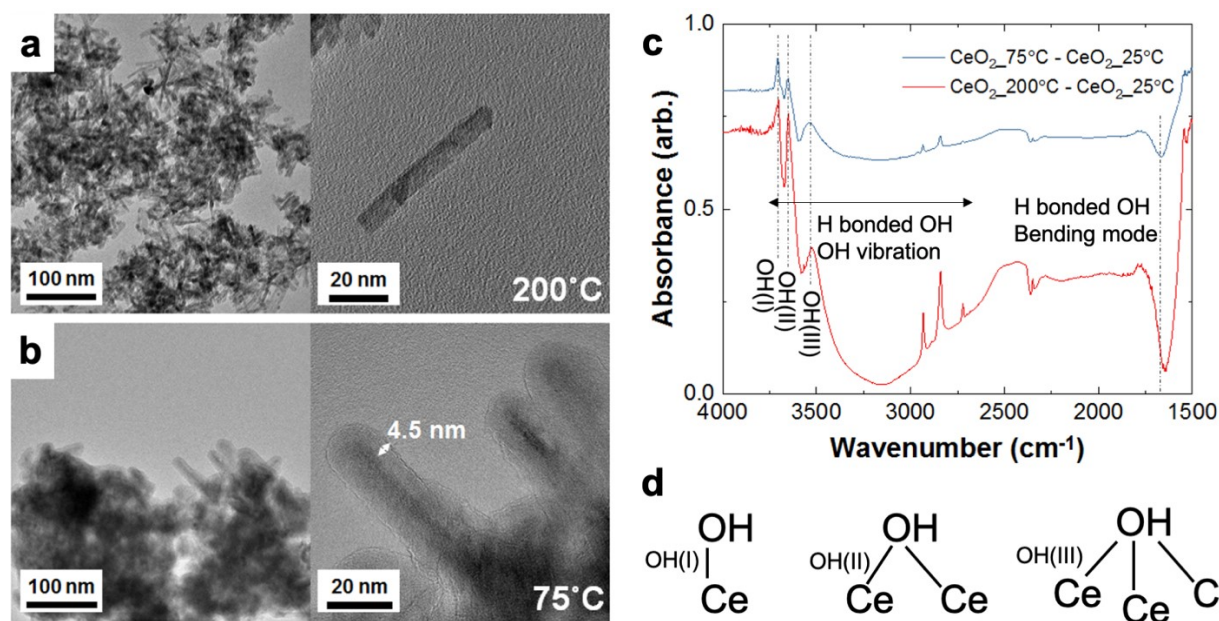


Figure 6. TEM images of $\text{CeO}_2\text{NRs}/45\text{Al}_2\text{O}_3$ generated at (a) 200 °C and (b) at 75 °C via the same ALD Al_2O_3 time sequence and (c) Differential DRIFTS spectra of CeO_2 NRs at 75 °C and 200 °C with DRIFTS spectrum of CeO_2NRs at 25 °C as the reference spectrum. (d) Molecular configurations of isolated OH groups, OH(I) mono-coordinated OH, OH(II) bridge OH, and OH(III) triple-bridge OH. No amorphous Al_2O_3 shell can be seen on $\text{CeO}_2\text{NRs}/45\text{Al}_2\text{O}_3$ that was generated at 200 °C, while an Al_2O_3 shell of ~4.5 nm thick can be observed on the sample that was generated at 75 °C. The positive peaks at 2928, 2833, and 2720 cm^{-1} are due to the movement of adsorbed carbon species, which we did not remove through oxidization at high temperatures as such treatment deforms CeO_2 NRs. The DRIFTS spectra show significant reduction of hydrogen bonded –OH peak (~2500–3600 cm^{-1}) from 75 °C to 200 °C and generation of isolated –OH groups.

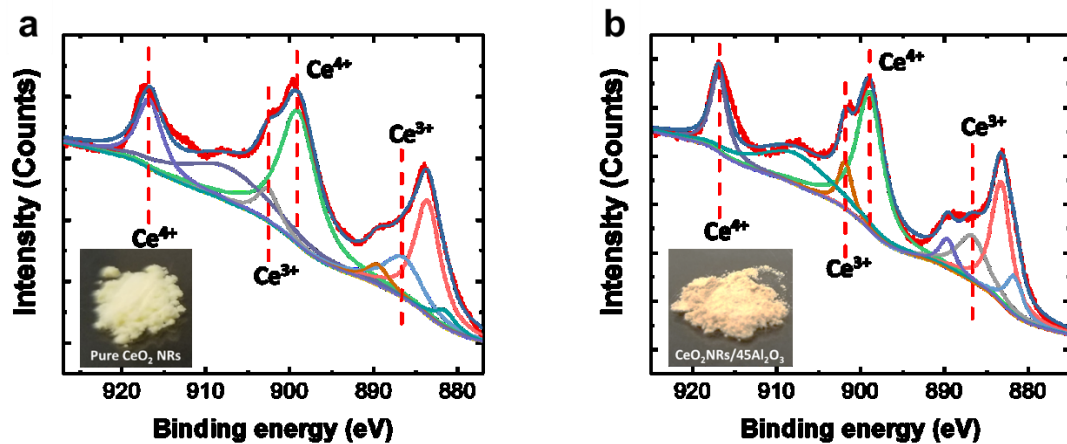


Figure 7. XPS spectra of (a) CeO_2 NRs and (b) $\text{CeO}_2\text{NRs}/45\text{Al}_2\text{O}_3$. The concentration of Ce^{3+} increased after 45 Al_2O_3 ALD cycles at 200 °C. CeO_2 has been reduced, more O vacancies created. The inset images show the color of the corresponding samples. $\text{CeO}_2\text{NRs}/45\text{Al}_2\text{O}_3$ is darker than CeO_2 NRs, indicating higher concentration of Ce^{3+} .

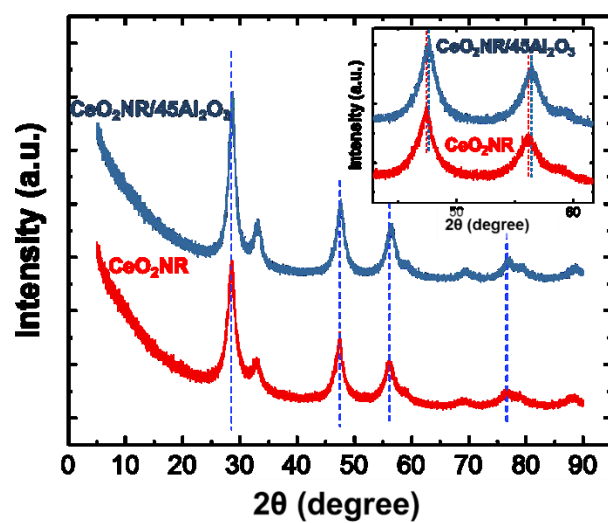


Figure 8. XRD spectra of CeO_2 NRs (bottom) and $\text{CeO}_2\text{NRs}/45\text{Al}_2\text{O}_3$ (top). XRD peaks shifted to higher 2θ after 45 cycles Al_2O_3 ALD at 200 °C, suggesting that the lattice constant of $\text{CeO}_2\text{NRs}/45\text{Al}_2\text{O}_3$ is smaller than that of CeO_2 NRs.

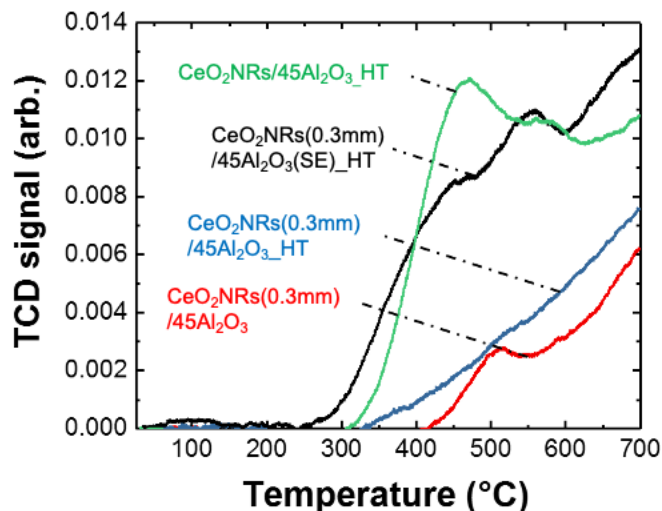


Figure 9. H₂ TPR of various CeO₂NRs/45Al₂O₃ samples with different treatment conditions. CeO₂NRs/45Al₂O₃_HT is obtained on 3 mm thick CeO₂ NRs powder-bed with 300 s TMA exposure and 20 s water dose each cycle, followed by HT. CeO₂NRs(0.3mm)/45Al₂O₃_HT and CeO₂NRs(0.3mm)/45Al₂O₃ are obtained on 0.3 mm CeO₂ NRs powder-bed with 300 s TMA exposure and 20 s water dose each cycle, with and without HT. CeO₂NRs(0.3mm)/45Al₂O₃(SE)_HT is obtained on 0.3 mm CeO₂ NRs powder-bed with short exposure (SE) of ALD reactants, i. e., 30 s TMA exposure and 2s water dose each ALD cycle, then followed by HT. The temperature ramping rate in TPR is 10 °C/min.